Revisiting the capacity-fading mechanism of P2-type sodium layered oxide cathode materials during high-voltage cycling

Meidan Jiang [a], Guannan Qian [a,b], Xiao-Zhen Liao [a,*], Zhouhong Ren [c], Qingyu Dong [d], Dechao Meng [a], Guijia Cui [a], Siqi Yuan [a], Sang-Jun Lee [b], Tian Qin [c], Xi Liu [c,*], Yanbin Shen [d], Yu-Shi He [a], Liwei Chen [c], Yijin Liu [b], Linsen Li [a,e,*], Zi-Feng Ma [a]

[a] Department of Chemical Engineering, Shanghai Electrochemical Energy Device Research Center (SEED), School of Chemistry and Chemical Engineering, Frontiers Science Center for Transformative Molecules, Shanghai Jiao Tong University, Shanghai 200240, China
[b] Stanford Synchrotron Radiation Lightsource, SLAC National Accelerator Laboratory, Menlo Park, CA 94025, United States
[c] In-Situ Center for Physical Sciences, School of Chemistry and Chemical Engineering, Shanghai Jiao Tong University, Shanghai 200240, China
[d] Suzhou Institute of Nanotech and Nanobionics (SINANO), Chinese Academy of Sciences, Suzhou 215123, Jiangsu, China
[e] Shanghai Jiao Tong University Sichuan Research Institute, Chengdu 610213, Sichuan, China

ARTICLE INFO

Article history:
Received 28 October 2021
Revised 31 December 2021
Accepted 6 January 2022
Available online 13 January 2022

Keywords:
Phase transition
Layered cathode
Buckling
Capacity fading mechanism
Sodium-ion batteries

ABSTRACT

P2-type sodium layered oxide cathode ($Na_{2/3}Ni_{1/3}Mn_{2/3}O_2$, P2-NNMO) has attracted great attention as a promising cathode material for sodium ion batteries because of its high specific capacity. However, this material suffers from a rapid capacity fade during high-voltage cycling. Several mechanisms have been proposed to explain the capacity fade, including intragranular fracture caused by the P2-O2 phase transion, surface structural change, and irreversible lattice oxygen release. Here we systematically investigated the morphological, structural, and chemical changes of P2-NNMO during high-voltage cycling using a variety of characterization techniques. It was found that the lattice distortion and crystal-plane buckling induced by the P2-O2 phase transition slowed down the Na-ion transport in the bulk and hindered the extraction of the Na ions. The sluggish kinetics was the main reason in reducing the accessible capacity while other interfacial degradation mechanisms played minor roles. Our results not only enabled a more complete understanding of the capacity-fading mechanism of P2-NNMO but also revealed the underlying correlations between lattice doping and the moderately improved cycle performance.

1. Introduction

Sodium-ion batteries (SIBs) have attracted great attention as a replacement for lithium-ion batteries (LIBs) because of the inexpensive and earth abundant sodium resources. Searching for high-performance cathode materials is important for developing advance SIBs. Various cathode materials, such as layered oxides [1–6], polyanionic compounds [7–12] and Prussian blue analogues [13–17] have been intensively explored. Among them, the layered transition-metal (TM) oxides Na_xTMO_2 ($0 < x < 1$) have attracted much attention due to their favorable electrochemical properties [1,18–24]. According to the oxygen stacking ordering and Na ion occupation sites, the layered sodium TM oxides can be categorized into P2 and O3 types, in which the Na ions occupy the octahedral (O) or trigonal prismatic (P) sites between the transition metal oxide TMO_2 layers, while the "2" or "3" refers to the number of alkali layers in the repeating unit [25]. The P2 structure provides more spacious diffusion paths for Na ions and generally show better rate performance [26–28]. One typical example is P2-$Na_{0.67}Ni_{0.33}Mn_{0.67}O_2$ (P2-NNMO), which has received significant attention due to its high working voltage and a large specific capacity. However, the P2-NNMO cathodes show a rapid capacity fade during high-voltage operation (>4.2 V vs. Na^+/Na) [29–31].

Much research work has been focused on understanding the capacity-fading mechanism of P2-NNMO to guide the development of improvement strategies [32–40]. Dahn et al. first investigated the Na^+ extraction/insertion behavior of P2-NNMO by *in situ* X-ray diffraction in 2001 [41]. Their work indicated that all of the Na^+ ions could be extracted from/inserted into $Na_{0.67}Ni_{0.33}Mn_{0.67}O_2$ when the material was cycled between 2.5 and 4.5 V. The cathode material retained the P2 structure when $\times > 1/3$ in $Na_xNi_{0.33}Mn_{0.67}O_2$. However, P2 and O2 phases co-existed with some stacking

* Corresponding authors.
E-mail addresses: liaoxz@sjtu.edu.cn (X.-Z. Liao), liuxi@sjtu.edu.cn (X. Liu), linsenli@sjtu.edu.cn (L. Li).

faults when $\times$ < 1/3. Since then, it was generally suggested by many researchers that the P2-O2 phase transition is associated with the structure degradation and fast capacity fading during cycling of P2-NNMO [29,31,40,42–45].

Recently, another degradation mechanism related to the lattice oxygen release at the high-voltage region is proposed [43,46–49]. In 2017, Ma et al. explored the oxygen activity in a high sodium-content and TM-deficient P2-$Na_{0.78}Ni_{0.23}Mn_{0.69}O_2$ material [46]. They proposed that the oxygen ions are involved in the charge compensation process at the high-voltage plateau. In 2018, Risthaus et al. reported a high discharge capacity (228 mAh g^{-1}) of P2-type $Na_{2/3}Ni_{1/3}Mn_{2/3}O_2$ cathode in 1.5–4.5 V [48]. This work indicated that the high capacity could be attributed to the redox activities of Ni ions, surface Mn ions and oxygen ions. The decomposition of the electrolyte led to the poor cycling performance, rather than the P2 to O2 phase transitions. In 2020, Zhang et al. reported that the capacity of P2-NNMO at the 4.2 V plateau was attributed to the irreversible $O^{2-}/O_2^{n-}/O_2$ evolution [47]. They also observed oxygen release and surface lattice densification. They suggested that the formation of the inactive rock-salt like phase was the main reason for the large irreversible capacity loss at the initial cycle. The effect of the P2-O2 phase transition was not discussed in this work.

Considering the non-negligible effect of the P2-O2 transition on the P2-NNMO cathode reported in the early literatures [26,33,50–53], we suppose that there must be some coupling effect of the detrimental P2-O2 transition and the surface side reactions, which collectively determines the structural stability and the electrochemical performance. To understand the structure-performance relationship in P2-NNMO cathode, we synthesized microsized P2-$Na_{0.64}Ni_{0.32}Mn_{0.68}O_2$ particles and investigated the morphological, chemical, and structural evolutions of the cathode material upon electrochemical cycling through a suite of characterization techniques. We observed that the P2-O2 phase transition during cycling of the P2-NNMO cathode not only led to a high density of intragranular micro-cracks but also severe crystal-plane buckling, which has been overlooked in previous studies. The cracks exposed the internal fresh surfaces, which aggravates the surface-related capacity-fading mechanisms such as TM dissolution and surface oxygen release. However, they are not the major contributor to the rapid capacity fading. We show that the large fraction of the capacity loss is due to kinetic limitation rather than active Na loss. Simply speaking, the Na ions are increasingly difficult to be extracted from the cathode material during the high-voltage operation, which is closely related to the crystal-plane buckling. The cycle performance of P2-NNMO can be moderately improved via aluminum (Al) doping, which suppressed the P2-O2 phase transition and resulted in less crystal-plane buckling. Our results highlight the importance of controlling interplanar gliding in improving the cycle performance of the sodium layered oxide cathode materials.

2. Experimental

2.1. Materials synthesis

In order to prepare a large particle single crystal pure phase P2-$Na_{0.67}Ni_{0.33}Mn_{0.67}O_2$ sample, a molten-salt-based method was applied in this work. The sodium molybdate (AR, 96.6%) was used as the flux and mixed with a stoichiometric mixture of Na_2CO_3 (with 2% excess of sodium, AR, 99.8%), $Ni(OH)_2$ (AR, 96.3%), and MnO_2 (AR, 99%). For preparing a Al-doped sample, 5% (in molar ratio) $Ni(OH)_2$ was substituted with Al_2O_3 (AR, γ-phase, 20 nm) in the precursor mixture. In the typical preparing process, the evenly mixed raw materials were calcinated at 1000 °C for 15 h. The calcined mixtures were grinded after cooling and washed away the molten salt by deionized water. After a further calcination at 750 °C for 10 h the final product samples were obtained.

2.2. Materials characterization

The chemical composition of the prepared samples was examined by the inductively coupled plasma optical emission spectrometer (ICP-OES, iCAP6300, USA). Elemental valence states of the material were determined by X-ray photoelectron spectroscopy (XPS, AXIS UltraDLD) using Al K_α (hv = 1486.6 eV) radiation. The morphology of the samples was observed by field emission scanning electron microscopy (Nova NanoSEM NPE218, FEI Company). Transmission electron microscopy (TEM) studies were performed using FEI Titan Themis Z electron microscope operating at 300 kV, using a high-angle annular detector resulting in 'Z-contrast' images. We aligned it by a standard gold sample before observations, which was corrected by probe SCOR spherical aberration corrector. The energy dispersive X-ray spectroscopy (EDS) mappings were carried out by four super X detectors. EELS spectra were acquired with an acquisition time of 1 s and a collection angle of 35 mrad.

The crystal structures of the samples were characterized using powder X-ray diffraction with a Bruker D8 Advance Power X-ray diffractometer (PXRD) at a scan rate of 1° min^{-1} in a 2 theta range of 10° to 80°, using Cu K_α radiation (λ = 0.154056 nm). For *in-situ* XRD experiment, the electrode was placed behind an X-ray transparent Be window. The signals were collected in a still mode with a planar detector during the charge/discharge process and each pattern was obtained in 18.2 min. The cathode was composed of active material, acetylene black, and polyvinylidene fluoride binder with a mass ratio of 8:1:1. The loading mass of the active material was 3.0–4.0 mg cm^{-2}.

Soft XAS measurements were performed in both total electron yield (TEY) and fluorescence yield (FY) modes on beamline 10-1 at Stanford Synchrotron Radiation Lightsource (SSRL) of the SLAC National Accelerator Laboratory, USA. The pristine and charged (4.0 and 4.3 V) electrodes were put on aluminum sample holder with double sided carbon tape in an argon filled glove box and then inserted in the experimental XAS chamber. Data were collected at room temperature under ultrahigh vacuum (10^{-9} Torr) using the total electron yield (TEY) and fluorescence yield (FY) mode detectors.

2.3. Electrochemical test

The electrochemical tests were carried out using coin cells (R2025) with Na metal foil as the counter electrode and using 0.8 M $NaPF_6$/PC + EMC + FEC + PST + DTD (40:56:2:1:1, v/v) as electrolyte. The cathode was composed of 80 wt% active material, 10 wt% super P and 10 wt% polyvinylidene fluoride (PVDF) binder. The coin type cells were assembled in an argon-filled glove box. Cycle performance of the cells was evaluated using a battery test system (Neware - BTS). The cyclic voltammetry of the cells was performed on an electrochemical analyzer (CH Instrument Co., Model 604D). Electrochemical impedance spectroscopy (EIS) was performed in a frequency range from 100 kHz to 0.01 Hz with an AC voltage amplitude of 10 mV.

3. Results and discussion

3.1. Structural characterizations of P2-NNMO

We prepared the P2-NNMO sample via a molten-salt method (see Experimental Section for details). The molten-salt reaction

medium promotes ion diffusion, which is favorable for growing microsized crystallites. Induced-couple plasma spectroscopy measurements indicated that the actual composition was $Na_{0.64}Ni_{0.32}Mn_{0.68}O_2$, which is close to the designed stoichiometry. Fig. 1(a) shows that the as-made particles were well-faceted and a few microns in particle size. The structure characterization was carried out using powder X-ray diffraction (XRD) analysis. The XRD pattern of $Na_{0.64}Ni_{0.32}Mn_{0.68}O_2$ displays Bragg diffraction peaks of a typical P2-type structure ($P6_3/mmc$ space group, Fig. 1b). The lattice parameters obtained via Rietveld refinements are $a = b = 2.8830$ Å, $c = 11.1871$ Å, $\alpha = \beta = 90°$, and $\gamma = 120°$. The high angle annular dark field (HAADF) image of the surface region of a P2-NNMO particle shows a highly ordered layered structure without any stacking faults (Fig. 1c). Additional scanning transmission electron microscope (STEM) images of the P2-NNMO particles can be seen in Fig. S1. Elemental mapping was also carried out using a STEM, which showed uniform distribution of Na, Ni, Mn, and O in the selected P2-NNMO particle. In this work, we used the P2-NNMO particles as a model system in studying the capacity-fading mechanism of P2-type sodium layered oxide cathodes.

3.2. Electrochemical performance of P2-NNMO

The electrochemical performance of the P2-NNMO cathode material was investigated in half cells using Na metal as the counter electrode. Fig. 2(a) displays the cycling performance of P2-NNMO in two separate voltage windows. When P2-NNMO was cycled in 4.0–2.0 V, it retained more than 95% of the initial capacity after 200 cycles (also see voltage profiles in Fig. 2b). Increasing the high cut-off voltage from 4.0 to 4.3 V led to a higher specific capacity of 160.6 mAh g^{-1}. However, a rapid capacity fade was observed during the high-voltage operation (Fig. 2a). The P2-NNMO cathode only retained a specific capacity of 77.1 mAh g^{-1} after 50 cycles in 4.3–2.0 V, which is consistent with previous results. Fig. 2(c) shows the voltage profiles of the P2-NNMO cathode at the 1st, 5th, 10th, 50th, and 100th cycles, in which several voltage plateaus could be observed. During the high-voltage cycling, the high-voltage plateau above 4.0 V shortened rapidly. Cyclic voltammetry (CV) tests were also performed on the P2-NNMO cathode in 4.3–2.0 V at a scan rate of 0.1 mV s^{-1}. Comparing the CV curves from the first 5 cycles also showed that the high-voltage redox peaks decreased significantly in intensity upon cycling (Fig. 2d), which is consistent from the galvanostatic cycling results shown in Fig. 2(c).

EIS measurements were also performed before and after cycling at the discharged state (Fig. 2e). We chose to focus on the initial cycles because the capacity fading of P2-NNMO was quite fast. The total impedance increased significantly in just five cycles and a second semi-circle was observed in the EIS spectra. The incline line in the low-frequency region, which is generally attributed to Li^+ diffusion in the solid material, was no longer visible. These results strongly suggest that the electrochemical reaction kinetics were altered during the high-voltage cycling of P2-NNMO.

3.3. Morphological changes of the P2-NNMO particles after cycling

To understand the rapid capacity fade during the high-voltage cycling, we first performed SEM observation on the cross-section of the P2-NNMO cathode after 10 cycles in 4.3–2.0 V. We chose the sample after the 10th cycle as the model system to study the capacity-fading mechanism because it had lost a significant amount of capacity (>30%). We hypothesized that the large capacity loss should accompany some major morphological, chemical, and/or structural changes. The sample cross-section was prepared via argon ion milling. Microcracks were observed in most of the P2-NNMO particles (Fig. 3a), which can be better seen in the STEM image shown in Fig. 3(b). It appears that the cracks were initiated from the surface and the crystal lattice was distorted near the fracture tip (Fig. 3c). It has been previously suggested that the intragranular fracture was a result of P2-O2 phase transition occurring at the high-voltage plateau [29]. To confirm this view-

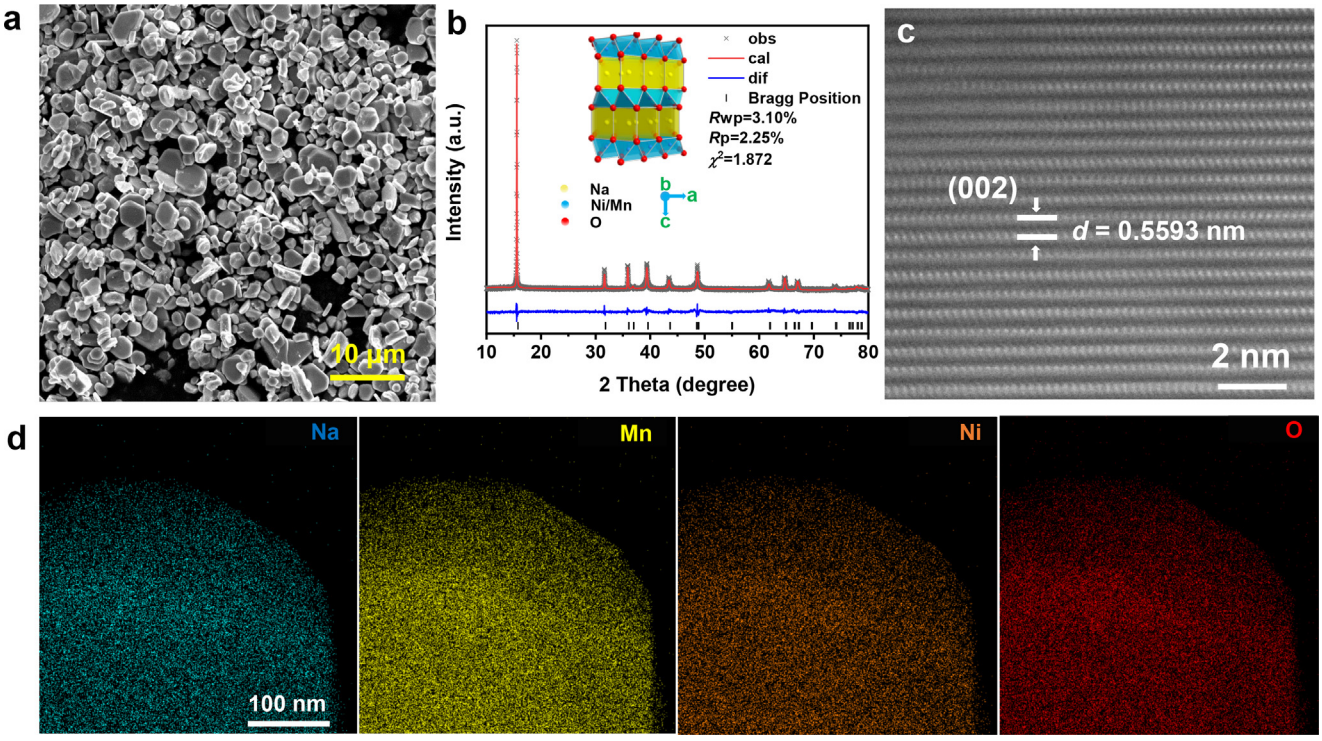

Fig. 1. Structural characterizations. (a) SEM image of the $Na_{0.64}Ni_{0.32}Mn_{0.68}O_2$ particles. (b) XRD pattern and rietveld refinement results. Inset is a schematic illustration of the P2-$Na_{0.64}Ni_{0.32}Mn_{0.68}O_2$ crystal structure. (c) HRTEM images. (d) STEM-EDS mapping.

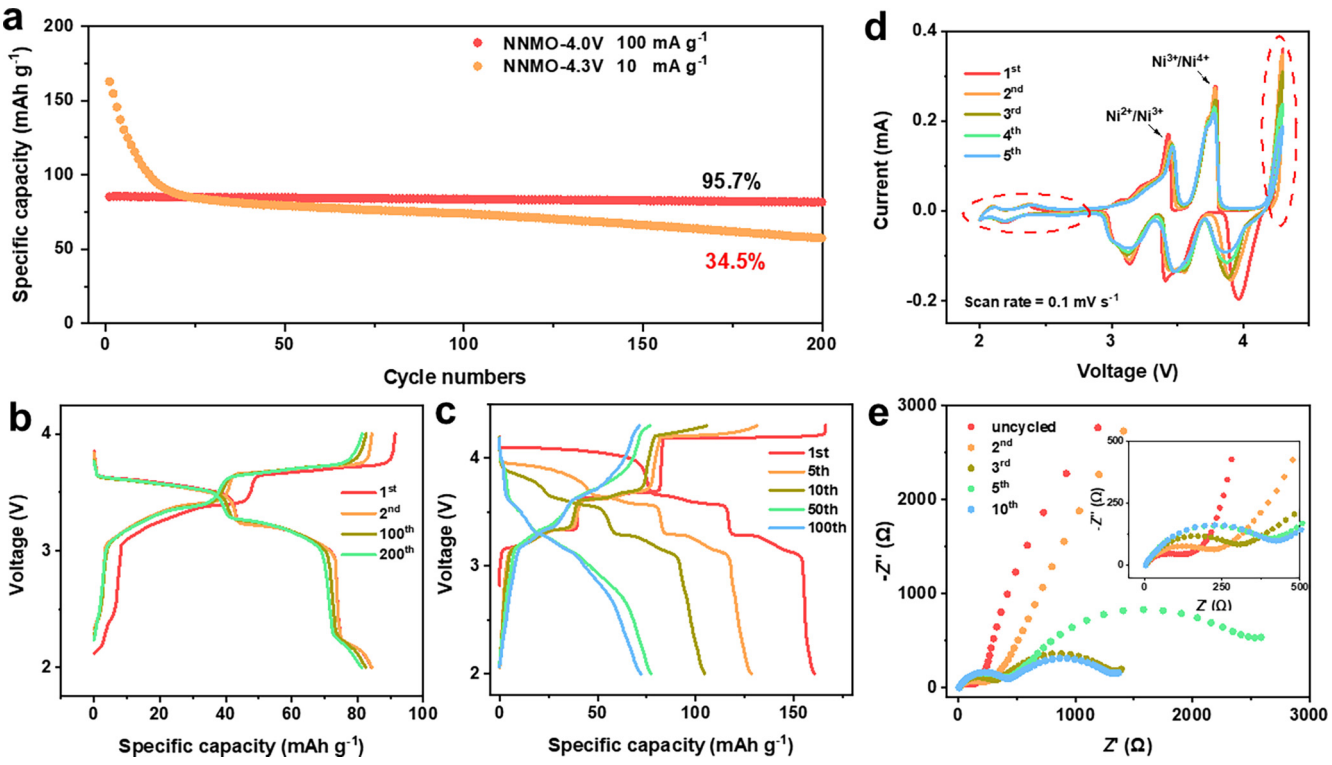

Fig. 2. Electrochemical performance. (a) Cycling performance between 2.0 and 4.3 V at a current density of 10 mA g^{-1} and between 2.0 and 4.0 V at a current density of 100 mA g^{-1}. The charge/discharge voltage profiles of $Na_{0.64}Ni_{0.32}Mn_{0.68}O_2$ cathode between 2.0 and 4.0 V at a current density of 100 mA g^{-1} (b) and within 2.0–4.3 V at a current density of 10 mA g^{-1} (c). (d) The cyclic voltammetry curves of $Na_{0.64}Ni_{0.32}Mn_{0.68}O_2$ between 2.0 and 4.3 V vs. Na/Na^+ at a scan rate of 0.1 mV s^{-1}. (e) Impedance spectra of $Na_{0.64}Ni_{0.32}Mn_{0.68}O_2$ electrode before cycling and after different cycles between 2.0 and 4.3 V; the inset is a magnified view of the EIS plot.

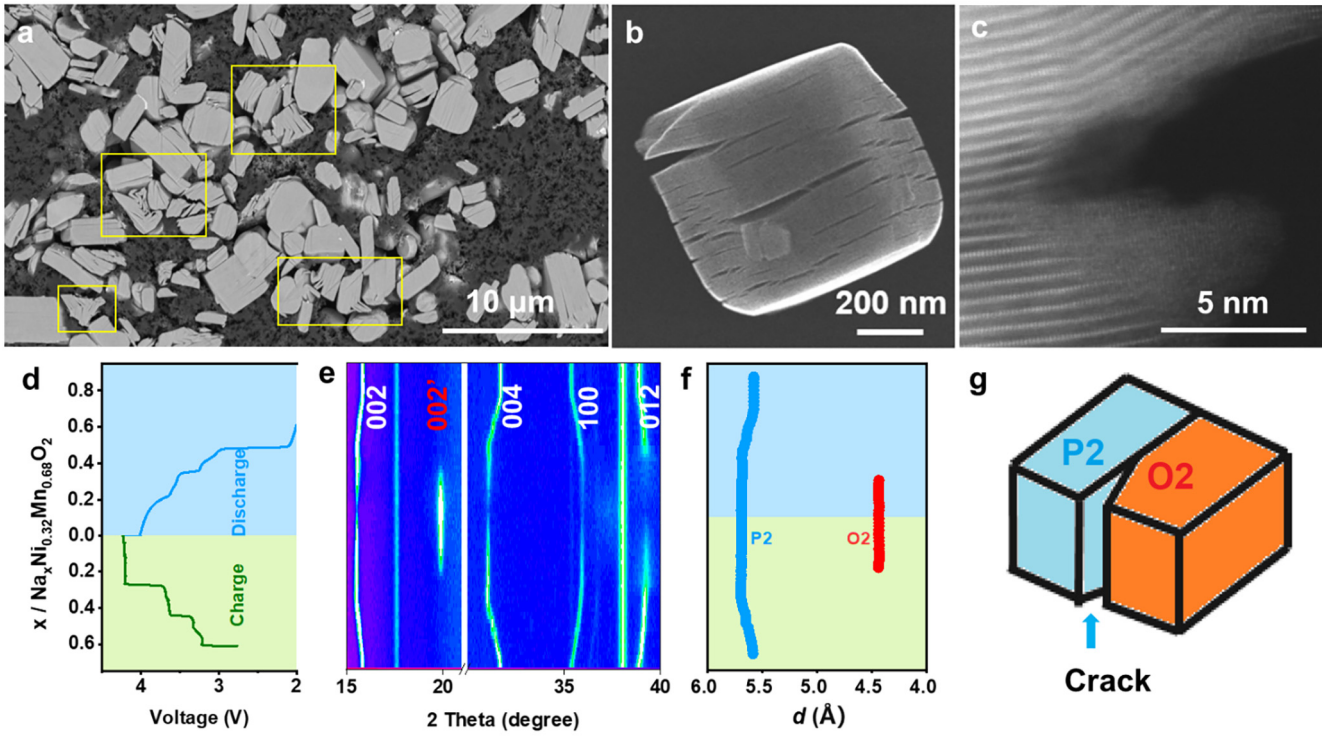

Fig. 3. (a) Cross sectional SEM images of electrode and (b) STEM images of particles after 10 cycles between 2.0 and 4.3 V. (c) HRTEM images of a cycled P2-NNMO particle after three cycles. (d) Charge/discharge voltage profile between 2.0–4.3 V at a current density of 10 mA g^{-1}. (e) Contour plot of the *in situ* XRD patterns. (f) The evolution of the *d* parameter ($d = 1/2c$, *c* is the interplanar spacing) calculated from the *in situ* XRD results. (g) Schematic illustration of crack occurring between P2 and O2 phases.

point, we carried out *in situ* XRD measurement on our P2-NNMO cathode. XRD patterns were recorded continuously during charge and discharge at 0.1C (Fig. 3d) and shown using a contour plot in Fig. 3(e). The P2-O2 phase transition was indeed observed in our P2-NNMO sample. During charge, the O2 phase appeared at ~4.2 V and x = 0.23 in the Na_xNMO. During discharge, when the x > 0.204 in Na_xNMO, almost all the O2 phase peaks disappeared. The structure returned to the P2 phase and all the diffraction peaks associated with the P2 phase shifted back to their initial positions as the discharge process proceeded. The P2-O2 phase transition appeared to be reversible based on the XRD patterns. However, we note that there is a large mismatch in lattice parameters between the two phases. The (002) interplanar spacing is ~22% smaller in the O2 structure than that in the P2 structure (Fig. 3f). Such lattice misfit would lead to stress at the O2-P2 phase boundary and provide the driving force for the surface cracks to further propagate toward the interior of the P2-NNMO particle [29] (see the schematic illustration in Fig. 3g).

3.4. Chemical evolution during high-voltage cycling of P2-NNMO

The intragranular fracture of the P2-NNMO particles during the high-voltage cycling exposed more internal surface area, which may leads to more surface side reactions. The surface reactivity is dependent on the chemical states of the elements, which may vary as the electrochemical reaction proceeds. In order to clearly probe the oxidation-state changes of TM ions in the charge process of the P2-NNMO, we performed high-resolution soft X-ray absorption spectroscopy (sXAS) on the P2-NNMO electrodes as illustrated in Fig. 4. The Ni and Mn L-edge soft XAS spectra at different charged voltage states were measured in both total electron yield (TEY) and fluorescence yield (FY) mode. The FY mode has a probing depth of about 50 nm that may probe the bulk information. The TEY mode has a probing depth of 2–5 nm, which was applied to characterizing the material surface. Fig. 4(a and b) show the evolution of the fine structure of Ni-L edge. The two main peaks at the L3 and L2 edges are due to electronic transitions from the metal $2p_{3/2}$ and $2p_{1/2}$ core levels to an unoccupied $3d$ level, respectively. The two L3 split peaks $L3_{high}$ and $L3_{low}$ corresponding to the $Ni^{3+/4+}$ and Ni $^{2+}$ content, respectively. It can be seen that the ratio of $Ni^{3+/4+}$ gradually increased with the increasing of charge voltage both in the bulk and at the surface, indicating the $Ni^{2+}/Ni^{3+}/Ni^{4+}$ redox reaction occurs in the whole charge process. However, it is also noticed that for the pristine and 4.0 V-state sample, the intensity ratios of split $L3_{high}/L3_{low}$ in TEY and FY modes are similar, whereas for the 4.3 V-state sample, $L3_{high}$ peak intensity is higher in FY mode than in TEY mode indicating a decrease of nickel oxidation state at the surface, which might be caused by the surface side reaction. In contrast, the fine structure of Mn L-edge peaks in Fig. 4(c) (FY mode, bulk-probe) and Fig. 4(d) (TEY-mode, surface-probe) almost remain unchanged when charged to 4.0 and 4.3 V. The Mn ions remain in the 4+ oxidation state during the charging process, indicating that the tetravalent Mn ions are electrochemically inactive (both at the surface and in the bulk) but may contribute to the stabilization of the layered structure.

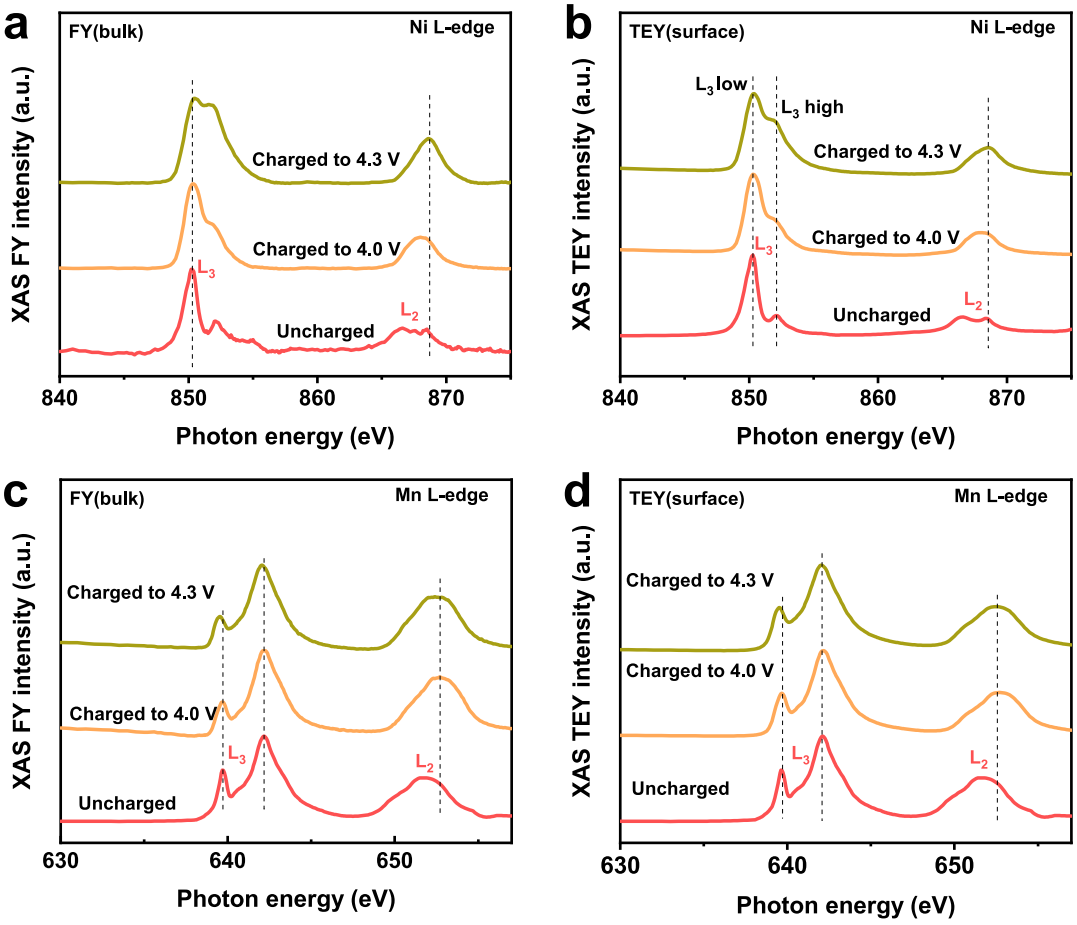

Fig. 4. High-resolution sXAS of the $Na_{0.64}Ni_{0.32}Mn_{0.68}O_2$ electrodes at different charged voltage states. fluorescence yield (FY) mode (a) and total electron yield (TEY) mode (b) of Ni L-edge evolution; fluorescence yield (FY) mode (c) and total electron yield (TEY) mode (d) of Mn L-edge evolution.

To further examine the chemical states of Ni and Mn ions at the surface, additional X-ray photoelectron spectroscopy (XPS) measurements were made on the P2-NNMO electrodes at three different states (i.e., pristine, charged to 4.0 V, and charged to 4.3 V). As shown in Fig. S2(a), the Ni 2*p* spectra of pristine electrode present a doublet of Ni $2p_{1/2}$ (872.03 eV) and Ni $2p_{3/2}$ (854.51 eV) peaks accompanied by two satellite peaks, indicating Ni^{2+}. Upon charging to 4.0 and 4.3 V, Ni^{2+} is oxidized to Ni^{3+} and Ni^{4+}. The Ni 2*p* XPS spectra at 4.0 and 4.3 V present a mixture of $Ni^{2+}/Ni^{3+}/Ni^{4+}$, while the ratio of Ni^{4+} increased after the P2-NNMO electrode was charged to 4.3 V. By contrast, the 2*p* XPS spectra of Mn (Fig. S2b) shows no obvious change during the charge process, implying that Mn^{4+} was inactive during charging. These results are consistent with those obtained from the TEY-mode sXAS measurements in Fig. 4(b and d).

In addition to the TM redox, we also investigated how the electronic state of oxygen changes during charging of the P2-NNMO electrode. Fig. 5(a) shows the O 1*s* XPS spectra at different charged states. For the pristine electrode, the deconvoluted O1*s* peak centered at 529.2 eV belongs to the lattice O^{2-}, the additional peaks at 531.05 and 532.95 eV are assigned to the surface oxygenated species. The charged electrodes show increased peak intensity of the surface oxygen species. When the electrode was charged to 4.3 V, a new component emerges at 530.5 eV, which can be attributed to the formation of $(O_2)^{n-}$ species according to several previous reports [46–48]. To further confirm the behavior of oxygen in the charge process, electron-energy loss spectroscopy measurements were made at the O K-edge for the pristine and charged particles both in the bulk and at the surface of the tested particles. It can be seen in Fig. 5(b and c) that the O K-edge peaks show no obvious change when the sample was charged to 4.0 V (compared to that of the pristine state) but show obvious change in the 4.3 V-state. The first peak of O K-edge (marked by a red dashed line) can be attributed to the electronic transition from the O 1*s* core state to the O 2*p*-TM 3*d* hybridized states [46,54]. This first peak of O K-edge show a small shift to higher energy when charged to 4.3 V in the bulk position, likely due to the oxidization of O^{2-} ion to O_2^{n-}. At the surface of 4.3 V particle, the first peak of O K-edge almost vanishes, indicating fewer holes in the 2*p*-3*d* hybridized orbitals. It likely means that the surface TMs are in a lower valence state [46], which is consistent with the Ni L-edge TEY-mode sXAS results in Fig. 4(b). Bringing together the above results from sXAS, XPS, and Electron Energy Loss Spectroscopy measurements, we can conclude that the $Ni^{2+}/Ni^{3+/4+}$ oxidation contributes to the charge-compensation in the low-voltage region (below 4.0 V), while the $Ni^{2+/3+}/Ni^{4+}$ and $O^{2-}/(O_2)^{n-}$ are involved in the high-voltage region (above 4.0 V). At the high voltage state, the oxidative Ni^{4+} and $(O_2)^{n-}$ ions on the electrode surface likely reacted with the electrolyte, which led to a gradient in the valence state of Ni ions from surface to the bulk at the charged state.

3.5. Capacity-fading mechanism of P2-NNMO

The P2-O2 phase transition in the high-voltage region led to the particle fracture, which created more surface area. As a result, the surface side reaction would intensify. In our sXAS measurements, we indeed observed that the oxidation state of Ni ions was lower at the surface compared to that in the bulk for the P2-NNMO electrode charged to 4.3 V (Fig. 4b), which suggested surface side reactions between the charged P2-NNMO electrode and the liquid electrolyte. In addition, we carried out ICP measurements on the cycled electrodes and observed loss of Mn and Ni compared to the pristine electrode (Fig. 6a), likely through dissolution. Mn and Ni dissolution from the particle surface would certainly contribute to the capacity fading. The surface lattice of the P2-NNMO cathode particles were distorted (Fig. 3c), which is likely related to the transition metal dissolution observed by the ICP measurements. Similar observations were also made by Wang et al in Ref. [29]. We also performed XRD analysis on a cycled electrode (after 50 cycles), which revealed a P2-type structure in the bulk (Fig. S3). All of the above results indicate that the performance degradation is mainly due to interfacial degradations, which seems to be in line with several previous reports [31,37–38,48,55]. However, in another previous work, Wang et al. clearly showed that the surface degradation layer has negligible effects on performance decay [29]. In Wang's work, their P2-NNMO cathodes showed little capacity loss when they were cycled below 4.1 V (below the high-voltage plateau) despite the formation of a thick surface degradation layer. Therefore, there must be other major factors in play with the capacity fading of the P2-NNMO during high-voltage cycling.

In our ICP measurements (Fig. 6a), we also noticed that the cycled P2-NNMO electrode, despite its large capacity loss (52%), had almost the same amount (wt%) of Na with the pristine electrode. To obtain particle-level information, time-of-flight secondary-ion mass spectroscopy (ToF-SIMs) imaging was per-

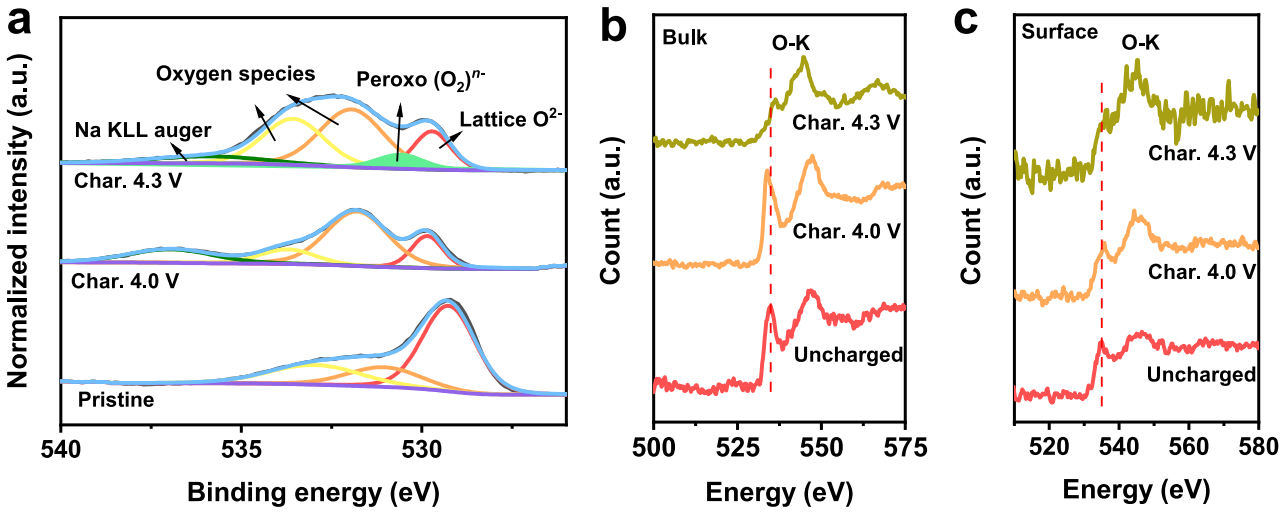

Fig. 5. (a) O 1*s* XPS spectra of the P2-NNMO cathodes. (b and c) The EELS spectra of the pristine $Na_{0.64}Ni_{0.32}Mn_{0.68}O_2$ and charged particles collected from the interior and the surface of the particles, respectively.

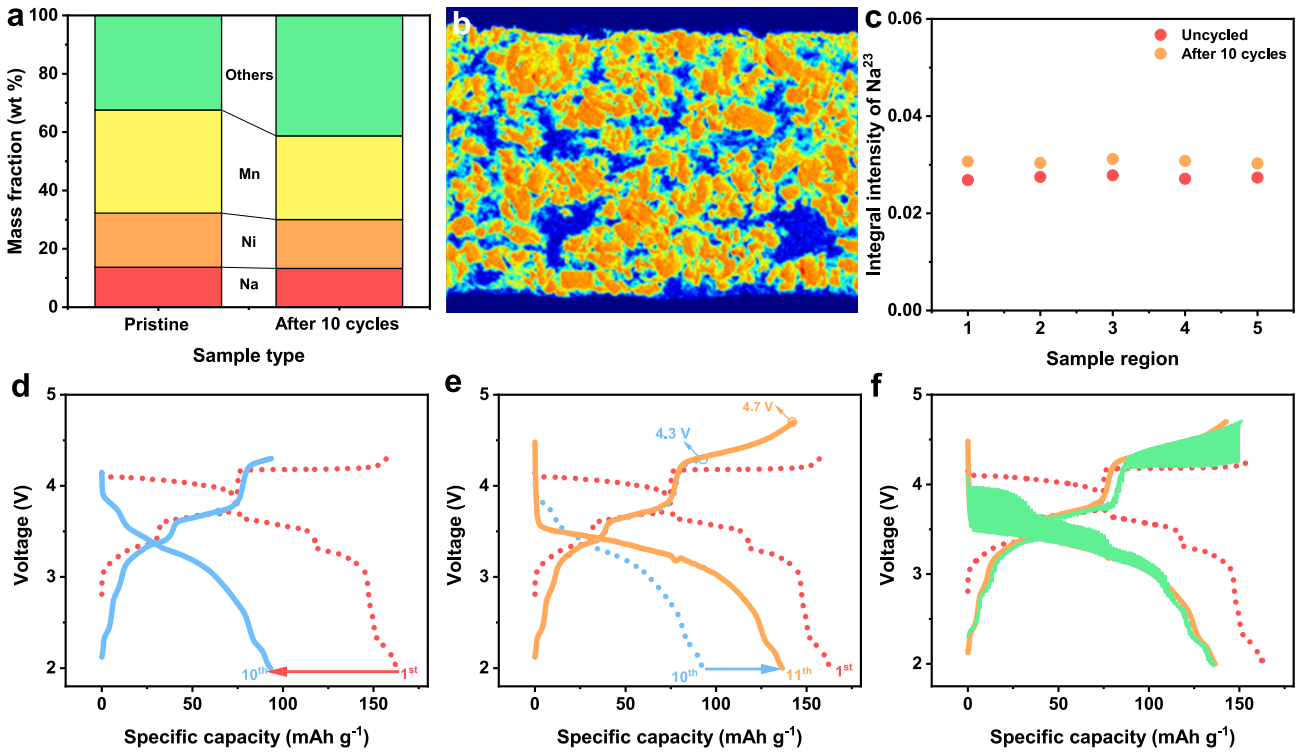

Fig. 6. (a) ICP results of a pristine P2-NNMO cathode and another one after 10 cycles. (b) Time-of-flight secondary-ion mass spectroscopy (ToF-SIMs) imaging performed on the cross-section of the 10-cycle electrode. (c) The integral intensity of the ToF-SIMs Na^{23} signals from several randomly selected regions. (d) First and tenth-cycle charge/discharge voltage profiles of P2-NNMO cathode within 2–4.3 V at a current density of 20 mA g^{-1}. (e) 11th charge/discharge voltage profile of P2-NNMO within 2.0–4.7 V. (f) GITT profile of P2-NNMO cathode tested between 2.0 and 4.7 V. Results in panels (d–f) were from the same piece of P2-NNMO electrode.

formed on the cross-section of the 10-cycle electrode, which revealed strong Na^{23} signal in all the particles (Fig. 6b). The integral intensity of the ToF-SIMs Na^{23} signals from several randomly selected regions in the 10-cycle electrode and the pristine electrode was actually comparable (Fig. 6c), which is consistent with the ICP results. It is clear now that the large capacity fade was not due to the loss of Na ions. Instead, Na ions were increasingly difficult to be extracted from the lattice during high-voltage cycling of the P2-NNMO electrode. This behavior is different from the Li-ion layered oxide cathode materials, in which case Li ions are difficult to be re-inserted into the lattice due to irreversible structural changes (such as the layered-to-rock salt phase transition).

It is now interesting to ask whether and how we can extract the Na ions from the high-voltage cycled P2-NNMO electrode, which displayed an apparently large capacity loss after 10 cycles during cycling in 4.3–2.0 V (~52% in Fig. 6d) and loss of the high-voltage plateau (~4 V). Two electrochemical protocols were applied to the same electrode. In the first one, we charged it to 4.7 V in the 11th cycle and then discharged it back to 2.0 V, which indeed recovered a significant amount of capacity despite the large polarization observed in the voltage profiles (Fig. 6e). After this, we applied a galvanostatic intermittent titration (GITT) protocol to the same electrode. In the GITT test, the electrode was charged for 30 min at 0.1C and then allowed to rest for 4 h. In literature, this method has been widely used to measure ion diffusivity. In this work, we used it to do "slow" charge and discharge and better discern the kinetic limitation. In Fig. 6(f), we can clearly see that large overpotentials exist during both charge and discharge. Interestingly, the cell voltage after the relaxation became closer to the high-voltage plateau at the first constant-current cycle, especially during the charge process. These electrochemical test results revealed that the apparently large capacity loss of the P2-NNMO electrode during high-voltage cycling was mainly due to kinetic limitations.

So what caused the large overpotential? We suggest that electron transport should not be a major factor in this case because that the P2-NNMO particles were not pulverized and still had electric contact with conductive carbon material after the high-voltage cycling (Fig. 3a). As for the Na ion transport, Wang's work has shown that the surface degradation layer does not impede Na-ion extraction and re-intercalation [29]. In our opinion, it is the lattice distortion and crystal-plane buckling (Fig. 3a–c and Fig. S4) in the bulk that significantly slow down the Na^+ transport and consequently caused the rapid capacity decay.

3.6. Lattice doping improves the cycle performance

The above results indicate that suppressing the P2-O2 phase transition at the high-voltage region is essential for improving its electrochemical performance. We chose to dope Al^{3+} ions into the crystal lattice of P2-NNMO with the hope that they can mitigate the interplanar gliding and the associated mechanical-induced damage. The Al-doped P2-NNMO sample was synthesized via the same method used for the undoped sample with Al_2O_3 as the Al source (see particle morphology in Fig. S5). The chemical composition of the Al-doped P2-NNMO was $Na_{0.608}Ni_{0.236}Mn_{0.702}Al_{0.054}O_2$ by ICP analysis. STEM-EDS mapping revealed uniform distribution of Na, Ni, Mn, Al, and O elements (Fig. S6). Rietveld refinement analysis indicated that Al-doped P2-NNMO sample exhibits the same crystal structure with the undoped one ($P6_3/mmc$ space group). The refined crystallographic data are listed in

Table S2. It can be seen that partial substitution of Al^{3+} for TM ions led to a slightly smaller *a*/*b* plane lattice constant.

In situ XRD measurement was made to evaluate the impact of the Al dopants on the phase transition kinetics during Na extraction and insertion (Fig. 7a). It is clear that the structural evolution of the Al-doped P2-NNMO cathode was different from the undoped one (Fig. 3d–f). A P2-OP4 phase transition was observed for the Al-doped sample (Fig. 7b), instead of the P2-O2 phase transition in the undoped P2-NNMO. The lattice mismatch was smaller for P2-OP4 than P2-O2. As a result, the Al-doped P2-NNMO cathode exhibited improved cycling performance over the undoped sample (Fig. 7e). The capacity retention was 72.8% and 45.7% for the Al-doped and the undoped P2-NNMO cathodes, respectively. We also carried out CV on the Al-doped P2-NNMO cathodes and compared the results with those obtained from the undoped P2-NNMO. In the CV tests, the high-voltage redox peaks in the Al-doped P2-NNMO decreased much slower than those in the undoped P2-NNMO (Fig. S7), which proved that the Al-doping improved the high-voltage stability. The improvement induced by Al-doping was also demonstrated in the GITT tests (Fig. S8). It is clear that the polarization was smaller in the Al-doped P2-NNMO sample after high-voltage cycling.

The intragranular fracture and crystal-plane buckling were mitigated in the Al-doped sample (but not completely suppressed), as shown by the cross-sectional SEM image of the Al-doped P2-NNMO electrode (Fig. 7f). This is why the Al-doped P2-NNMO cathode exhibited improved cycle performance over the undoped sample but still exhibited a relatively fast capacity fading rate.

It is clear now that the P2-O2 phase transition leads to cracks and crystal-plane buckling, which hinder Na-ion migration in the bulk and reduce the accessible capacity (Fig. 8). Doping the P2-NNMO lattice with Al^{3+} (in this work and also in a previous report [54]) and other dopants such as Mg [29,53], Cu [51], Fe [18,35] and Ti [56] are effective in suppressing the detrimental P2-O2 phase transition and the associated structural and mechanical degradations. As a result, a facile Na-ion transport can still be maintained.

4. Conclusions

In this work, we used a variety of characterization techniques to elucidate the capacity-fading mechanism of a P2-type Na layered oxide cathode materials (P2-NNMO) during high-voltage cycling (2.0–4.3 V) in Na-ion batteries. Although TM dissolution and surface structural changes contributed to the capacity fade, which would aggravate after the P2-NNMO particle fractured due to the P2-O2 phase transistion, they were not the major factor. The "apparently degraded" P2-NNMO cathode did not actually lose much Na. A large fraction of the capacity fade was due to sluggish Na-ion transport in the bulk, which was closely related to the lattice distortion and crystal-plane buckling. The Na ions could still be extracted with an additional overpotential or under a slow-charge condition. We further revealed the underlying correlation

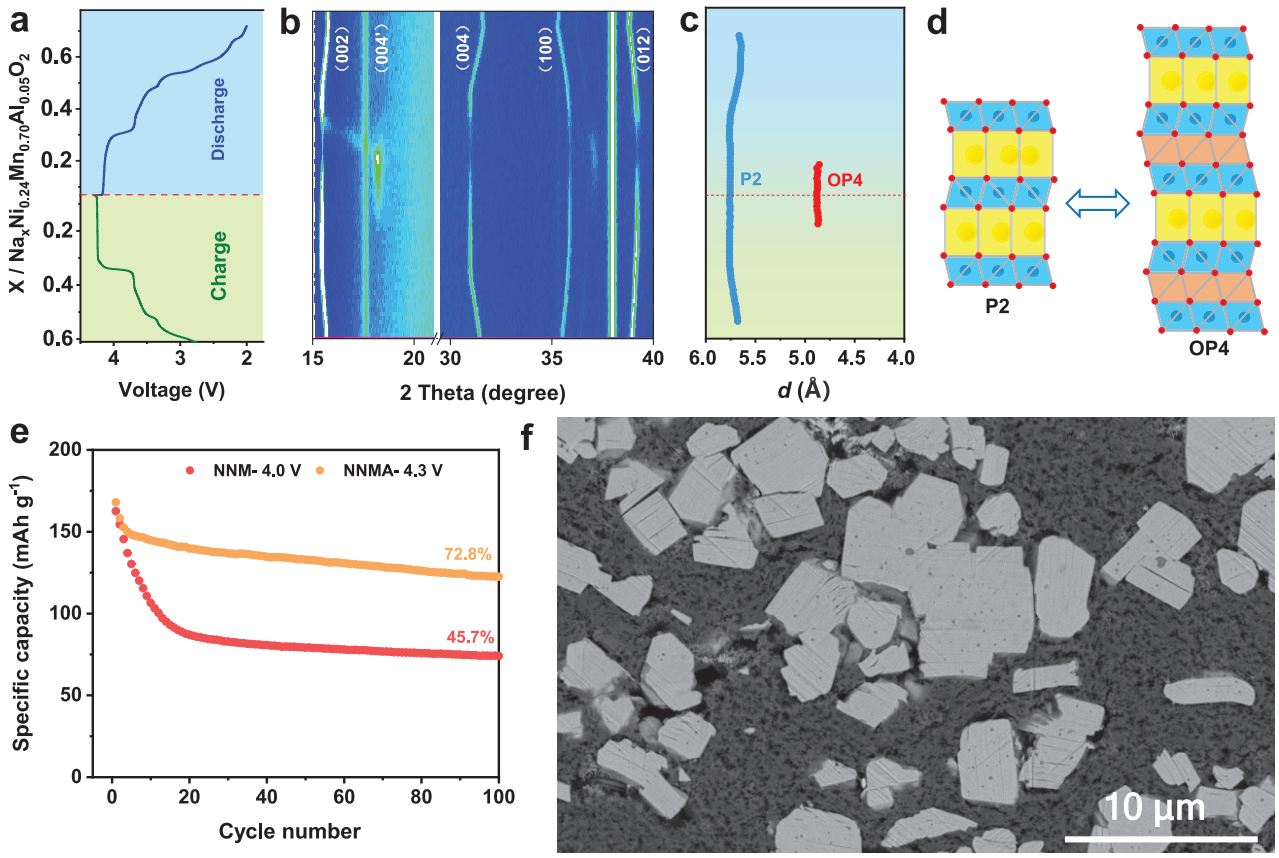

Fig. 7. (a) Charge/discharge voltage profile of the Al-doped P2-NNMO between 2.0–4.3 V at a current density of 10 mA g^{-1}; (b) contour plot of *in situ* XRD patterns; (c) the evolution of the *d* parameter (*d* = 1/4 lattice parameter *c*); (d) schematic illustration of P2-OP4 phase transition; (e) the cycling performance of Al-doped P2-NNMO ($Na_{0.608}Ni_{0.236}Mn_{0.702}Al_{0.054}O_2$ and P2-NNMO cathodes tested within 2–4.3 V at a current density of 10 mA g^{-1}; (f) cross-sectional SEM image of the NNMA electrode after 10 cycles. Less fracture and crystal-plane buckling were observed.

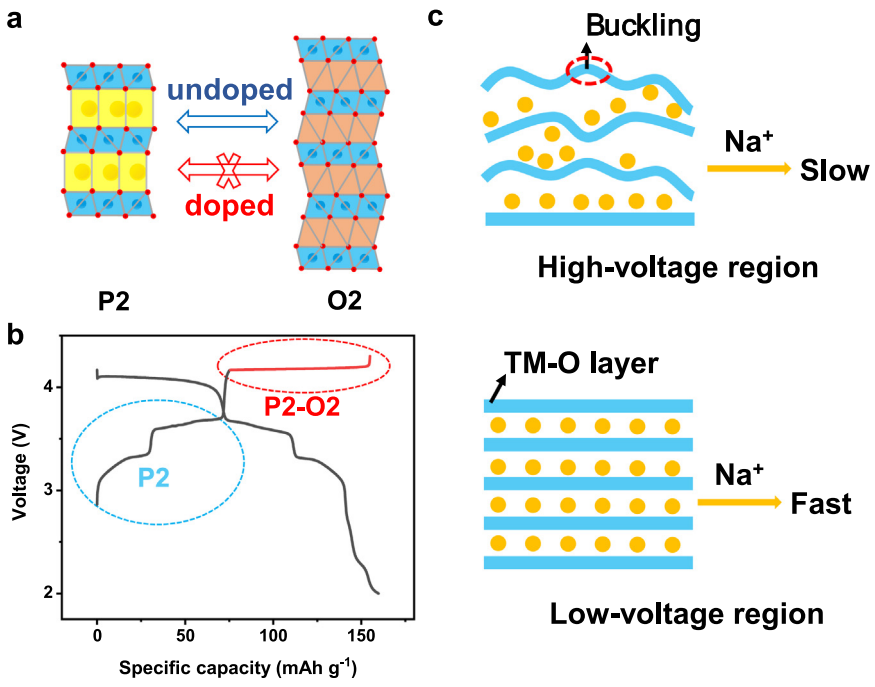

Fig. 8. (a) Illustration of P2-O2 phase transition. (b) The charge/discharge profile of P2-NNMO cathodes. (c) Schematic illustration showing the correlation between the structural change and Na-ion transport kinetics.

between the improved high-voltage cycle performance of the doped P2-NNMO cathode and the dopants' ability to suppress the P2-O2 phase transition. Our results provide a more complete understanding of the capacity fading mechanism of the P2-NNMO cathode during high-voltage cycling and highlight the importance of reducing bulk lattice distortion in layered oxide cathode materials.

Declaration of Competing Interest

The authors declare that they have no known competing financial interests or personal relationships that could have appeared to influence the work reported in this paper.

Acknowledgments

The authors gratefully acknowledge financial support from the National Natural Science Foundation of China (21938005, 21573147, 22005190, 22008154, 21872163), the Science & Technology Commission of Shanghai Municipality, the Natural Science Foundation of Shanghai (19DZ1205500, 19ZR1424600, 19ZR1475100), and the Sichuan Science and Technology Program (2021JDRC0015 to L.S.L). The authors also thank beamline 10-1 of SSRL (Stanford Synchrotron Radiation Lightsource) for providing beam time. Stanford Synchrotron Radiation Lightsource, SLAC National Accelerator Laboratory, is supported by the U.S. Department of Energy (DOE), Office of Science, Office of Basic Energy Sciences (DE-AC02-76SF00515).

Appendix A. Supplementary data

Supplementary data to this article can be found online at https://doi.org/10.1016/j.jechem.2022.01.010.

References

[1] K. Kubota, N. Yabuuchi, H. Yoshida, M. Dahbi, S. Komaba, MRS Bull 39 (2014) 416–422.
[2] C. Luo, A. Langrock, X. Fan, Y. Liang, C. Wang, J. Mater. Chem. A 5 (2017) 18214–18220.
[3] K. Kubota, S. Kumakura, Y. Yoda, K. Kuroki, S. Komaba, Adv. Energy Mater. 8 (2018) 1703415.
[4] Q. Wang, C. Zhao, Y. Lu, Y. Li, Y. Zheng, Y. Qi, X. Rong, L. Jiang, X. Qi, Y. Shao, D. Pan, B. Li, Y.S. Hu, L. Chen, Small 13 (2017) 1701835.
[5] C. Fang, Y. Huang, W. Zhang, J. Han, Z. Deng, Y. Cao, H. Yang, Adv. Energy Mater. 6 (2016) 1501727.
[6] F. Wei, Q. Zhang, P. Zhang, W. Tian, K. Dai, L. Zhang, J. Mao, G. Shao, J. Electrochem. Soc. 168 (2021) 050524.
[7] D. Wang, P. Cai, G.-Q. Zou, H.-S. Hou, X.-B. Ji, Y. Tian, Z. Long, Rare Metals 41 (2022) 115–124.
[8] Q. Ni, Y. Bai, F. Wu, C. Wu, Adv. Sci. 4 (2017) 1600275.
[9] H. Li, M. Xu, Z. Zhang, Y. Lai, J. Ma, Adv. Funct. Mater. 30 (2020) 2000473.
[10] S.K. Sapra, J. Pati, P.K. Dwivedi, S. Basu, J.-K. Chang, R.S. Dhaka, WIREs Energy Environ. 10 (2021) e400.
[11] Y. Niu, Y. Zhang, M. Xu, J. Mater. Chem. A 7 (2019) 15006–15025.
[12] Z. Lv, M. Ling, M. Yue, X. Li, M. Song, Q. Zheng, H. Zhang, J. Energy Chem. 55 (2021) 361–390.
[13] F. Peng, L. Yu, P. Gao, X.-Z. Liao, J. Wen, Y.-S. He, G. Tan, Y. Ren, Z.-F. Ma, J. Mater. Chem. A 7 (2019) 22248–22256.
[14] J. Peng, J. Wang, H. Yi, W. Hu, Y. Yu, J. Yin, Y. Shen, Y. Liu, J. Luo, Y. Xu, P. Wei, Y. Li, Y. Jin, Y. Ding, L. Miao, J. Jiang, J. Han, Y. Huang, Adv. Energy Mater. 8 (2018) 1702856.
[15] G. Du, H. Pang, Energy Storage Mater. 36 (2021) 387–408.
[16] J. Qian, C. Wu, Y. Cao, Z. Ma, Y. Huang, X. Ai, H. Yang, Adv. Energy Mater. 8 (2018) 1702619.
[17] B. Wang, Y. Han, X. Wang, N. Bahlawane, H. Pan, M. Yan, Y. Jiang, iScience 3 (2018) 110-133.
[18] D. Yuan, X. Hu, J. Qian, F. Pei, F. Wu, R. Mao, X. Ai, H. Yang, Y. Cao, Electrochim. Acta 116 (2014) 300–305.
[19] P.F. Wang, H.R. Yao, X.Y. Liu, J.N. Zhang, L. Gu, X.Q. Yu, Y.X. Yin, Y.G. Guo, Adv. Mater. 29 (2017) 1700210.
[20] H. Xu, J. Zong, X.-J. Liu, Ionics 24 (2018) 1939–1946.
[21] Y. Zhang, S. Kim, G. Feng, Y. Wang, L. Liu, G. Ceder, X. Li, J. Electrochem. Soc. 165 (2018) A1184–A1192.
[22] J. Zhao, X. Zhang, J. Wang, X. Yang, J. Deng, Y. Wang, J. Solid St. Electrochem. 24 (2020) 1349–1361.
[23] J. Zhao, X. Zhang, Q. Zhao, L. Wang, Y. Wang, Chem. Phys. 529 (2020) 110582.
[24] T.R. Chen, T. Sheng, Z.G. Wu, J.T. Li, E.H. Wang, C.J. Wu, H.T. Li, X.D. Guo, B.H. Zhong, L. Huang, S.G. Sun, ACS Appl. Mater. Interf. 10 (2018) 10147–10156.
[25] C.-D.-J.-J. Braconnier, C. Fouassier, P. Hagenmuller, Mater. Res. Bull. 15 (1980) 1979–11804.

[26] D.H. Lee, J. Xu, Y.S. Meng, Phys. Chem. Chem. Phys. 15 (2013) 3304–3312.
[27] Z.-Y. Li, J. Zhang, R. Gao, H. Zhang, L. Zheng, Z. Hu, X. Liu, J. Phys. Chem. C 120 (2016) 9007–9016.
[28] Y. Zhu, V. Pande, L. Li, B. Wen, M.S. Pan, D. Wang, Z.-F. Ma, V. Viswanathan, Y.-M. Chiang, Proc. Natl. Acad. Sci. USA 117 (2020) 27195–27203.
[29] K. Wang, P. Yan, M. Sui, Nano Energy 54 (2018) 148–155.
[30] X. Cai, Y. Xu, L. Meng, X. Wei, F. Xiong, T. Xiong, Q. An, J. Alloys Comp. 820 (2020) 153093.
[31] Y. Liu, X. Fang, A. Zhang, C. Shen, Q. Liu, H.A. Enaya, C. Zhou, Nano Energy 27 (2016) 27–34.
[32] G. Singh, N. Tapia-Ruiz, J.M. Lopez del Amo, U. Maitra, J.W. Somerville, A.R. Armstrong, J. Martinez de Ilarduya, T. Rojo, P.G. Bruce, Chem. Mater. 28 (2016) 5087–5094.
[33] D. Pahari, S. Puravankara, J. Power Sources 455 (2020) 227957.
[34] W. Zhao, H. Kirie, A. Tanaka, M. Unno, S. Yamamoto, H. Noguchi, Mater. Lett. 135 (2014) 131–134.
[35] Q. Yang, P.F. Wang, J.Z. Guo, Z.M. Chen, W.L. Pang, K.C. Huang, Y.G. Guo, X.L. Wu, J.P. Zhang, ACS Appl. Mater. Interf. 10 (2018) 34272–34282.
[36] S. Yuan, J. Qi, M. Jiang, G. Cui, X.Z. Liao, X. Liu, G. Tan, W. Wen, Y.S. He, Z.F. Ma, ACS Appl. Mater. Interf. 13 (2021) 3793–3804.
[37] J. Alvarado, C. Ma, S. Wang, K. Nguyen, M. Kodur, Y.S. Meng, ACS Appl. Mater. Interf. 9 (2017) 26518–26530.
[38] K. Tang, Y. Huang, X. Xie, S. Cao, L. Liu, M. Liu, Y. Huang, B. Chang, Z. Luo, X. Wang, Chem. Eng. J. 384 (2020) 123234.
[39] P.-F. Wang, Y. You, Y.-X. Yin, Y.-G. Guo, Adv. Energy Mater. 8 (2018) 1701912.
[40] K. Wang, H. Wan, P. Yan, X. Chen, J. Fu, Z. Liu, H. Deng, F. Gao, M. Sui, Adv. Mater. 31 (2019) e1904816.
[41] Z. Lu, J.R. Dahn, J. Electrochem. Soc. 148 (2001) A1225.
[42] P.F. Wang, Y. You, Y.X. Yin, Y.S. Wang, L.J. Wan, L. Gu, Y.G. Guo, Angew. Chem. Int. Ed. 55 (2016) 7445–7449.
[43] X. Wu, G.L. Xu, G. Zhong, Z. Gong, M.J. McDonald, S. Zheng, R. Fu, Z. Chen, K. Amine, Y. Yang, ACS Appl.Mater. Interf. 8 (2016) 22227–22237.
[44] L. Zheng, J. Li, M.N. Obrovac, Chem. Mater. 29 (2017) 1623–1631.
[45] J. Zhang, W. Wang, W. Wang, S. Wang, B. Li, ACS Appl. Mater. Interf. 11 (2019) 22051–22066.
[46] C. Ma, J. Alvarado, J. Xu, R.J. Clement, M. Kodur, W. Tong, C.P. Grey, Y.S. Meng, J. Am. Chem. Soc. 139 (2017) 4835–4845.
[47] Y. Zhang, M. Wu, J. Ma, G. Wei, Y. Ling, R. Zhang, Y. Huang, ACS Cent. Sci. 6 (2020) 232–240.
[48] T. Risthaus, D. Zhou, X. Cao, X. He, B. Qiu, J. Wang, L. Zhang, Z. Liu, E. Paillard, G. Schumacher, M. Winter, J. Li, J. Power Sources 395 (2018) 16–24.
[49] W. Zuo, F. Ren, Q. Li, X. Wu, F. Fang, X. Yu, H. Li, Y. Yang, Nano Energy 78 (2020) 105285.
[50] R.J. Clément, P.G. Bruce, C.P. Grey, J. Electrochem. Soc. 162 (2015) A2589–A2604.
[51] L. Wang, Y.-G. Sun, L.-L. Hu, J.-Y. Piao, J. Guo, A. Manthiram, J. Ma, A.-M. Cao, J. Mater. Chem. A 5 (2017) 8752–8761.
[52] I. Hasa, S. Passerini, J. Hassoun, J. Mater. Chem. A 5 (2017) 4467–4477.
[53] Y. Shi, S. Li, A. Gao, J. Zheng, Q. Zhang, X. Lu, L. Gu, D. Cao, ACS Appl. Mater. Interf. 11 (2019) 24122–24131.
[54] R. Dang, M. Chen, Q. Li, K. Wu, Y.L. Lee, Z. Hu, X. Xiao, ACS Appl. Mater. Interf. 11 (2019) 856–864.
[55] Z. Cao, L. Li, C. Zhou, X. Ma, H. Wang, Funct. Mater. Lett. 13 (2020) 2051010.